Applied Catalysis B: Environmental 312 (2022) 121392

Contents lists available at ScienceDirect

Applied Catalysis B: Environmental

journal homepage: www.elsevier.com/locate/apcatb

Pd-SnO_2 interface enables synthesis of syngas with controllable H_2/CO ratios by electrocatalytic reduction of CO_2

Haichuan He [a], Dan Xia [a], Xiao Yu [a], Jian Wu [a], Yan Wang [a], Liqiang Wang [b], Linlin Wu [a], Jianhan Huang [a], Ning Zhao [c], Liu Deng [a,*], You-Nian Liu [a,*]

[a] Hunan Provincial Key Laboratory of Micro & Nano Materials Interface Science, College of Chemistry and Chemical Engineering, Central South University, Changsha, Hunan 410083, PR China

[b] Henan Province Industrial Technology Research Institute of Resources and Materials, School of Material Science and Engineering, Zhengzhou University, Zhengzhou, Henan 450001, PR China

[c] State Key Laboratory of Coal Conversion, Institute of Coal Chemistry, Chinese Academy of Sciences, Taiyuan, Shanxi 030001, PR China

ARTICLE INFO

Keywords:
Pd-SnO_2 interface
Syngas
Controllable H_2/CO ratio
Electrochemical CO_2 reduction

ABSTRACT

Electrochemical CO_2 reduction reaction (eCO_2RR) to syngas (CO + H_2) is considered as a great potential and efficient way to abate carbon emissions and mitigate the depletion of fossil resources. Herein, a series of Pd-loaded SnO_2 nanosheets catalysts (Pd-SnO_2 NSs) are developed by photodeposition of Pd on the surface of SnO_2 nanosheets. Due to the formation of the active Pd-SnO_2 interface, the as-prepared Pd-SnO_2 catalysts exhibit a suppressed eCO_2RR to HCOOH pathway, thus realizing the faradaic efficiency of syngas close to 100%. The obtained optimal 4.3Pd-SnO_2 catalyst exhibits high CO selectivity (78% FE_{CO}) and wide H_2/CO ratio ranged from 4.2 to 0.28. Notably, the H_2/CO ratio can be controlled easily by adjusting the applied potential. Moreover, the H_2/CO ratio can maintain for more than 30 h. This work unfolds a promising candidate for earth-abundant Sn-based electrocatalysts for eCO_2RR to syngas.

1. Introduction

As an important raw material, syngas (CO + H_2) can produce various value-added chemical feedstocks and hydrocarbons through the industrial processes (e.g. Fischer-Tropsch synthesis) [1–5]. Traditionally, the industrial generation of syngas is primarily relied on the water-gas shift reaction of non-renewable fossil fuels (such as coal, oil, and natural gas), which requires huge energy investment and harsh conditions [6–9]. Therefore, to develop sustainable syngas production technique is highly required to substitute the facing-exhausted fossil fuels. The electrochemical CO_2 reduction reaction (eCO_2RR) is considered as the clean and promising method to produce CO [10–16]. Besides, the hydrogen evolution reaction (HER), which takes place in the same range of potentials as eCO_2RR as a competitive reaction, is also a green method to generate H_2 [17–22]. Taking the advantage of mild and controllable reaction condition during eCO_2RR process, syngas generation can greatly help reduce energy consumption and pollution. Moreover, if a CO:H_2 ratio can be controlled to the desired ratio for the existing thermo-catalytic process, for example, when the ratios of H_2/CO are 0.6 and 2, the syngas has been widely used for Fischer-Tropsch reaction and methanol synthesis [23–26]. Thus, growing efforts have been devoted to develop electrocatalysts for the transformation of CO_2 and H_2O towards syngas with controllable ratios and high activity.

To date, many metals and their oxide-derived nanomaterials (e.g., Ag, Au, Sn, Bi, etc.), have been investigated as electrocatalysts for eCO_2RR in search of a viable process for recycling CO_2 [27–30]. Among them, tin dioxide (SnO_2) represents one of the most promising catalysts, owing to its high-activity for eCO_2RR, low cost and environmentally friendly [31,32]. However, the efficiency of CO generation is greatly hampered by series of by-products, including formic acid, methane, methanol, etc [33–36]. Especially, the formation of high percentage of formic acid in the eCO_2RR on a tin-based catalyst consumes a lot of electricity, consequently, reduces the energy efficiency, which hinders efficient production of target syngas. Thus, a great deal of attention has been paid to the development of eCO_2RR catalysts that have high selectivity for CO and HER activity. It is widely accepted that the selectivity is highly dependent on the surface and interface electronic structure of catalysts, especially the local charge density redistribution of metals at active sites, which can be tailored through the doping of heteroatoms or interacting with foreign metal atoms [37–39]. For

* Corresponding authors.
E-mail addresses: dengliu@csu.edu.cn (L. Deng), liuyounian@csu.edu.cn (Y.-N. Liu).

https://doi.org/10.1016/j.apcatb.2022.121392
Received 22 January 2022; Received in revised form 23 March 2022; Accepted 6 April 2022
Available online 8 April 2022

example, Chen and co-workers constructed Sn−Ti−O interfaces for the electron-density transfer from Ti to Sn, which enhances the dissociative adsorption of *COOH intermediate and results in producing CO instead of HCOOH [13]. Zheng and co-workers demonstrated a 2D hierarchical Pd/SnO_2 structure met a demand on balancing CO adsorption and activation for electroreduction of CO_2 to CH_3OH via a multi-electron transfer process [36]. Though Pd shows high activity for eCO_2RR and HER, the strong CO adsorption limits its practical application [40,41]. Therefore, establishing a counterpoise Pd-SnO_2 interface to tailor the electronic structures of the active metal sites has great potential to control the eCO_2RR and HRE processes, suppressing the HCOOH selectivity, thus achieving the production of syngas with controllable H_2/CO ratios.

Herein, we develop a facile preparation of Pd-modified SnO_2 nanosheets catalysts (Pd-SnO_2 NSs) for efficient syngas production with widely tunable H_2/CO ratios. Large-size SnO_2 NSs provide a high specific area for supporting Pd nanoparticles, thereby exposing more active interface. With the increasing of Pd-SnO_2 interface, the eCO_2RR to HCOOH pathway is greatly suppressed. Pd-SnO_2 NSs display high activity, as well as desirable current density and stability for CO_2 reduction to CO. Most importantly, the ratios of CO to H_2 in the products can be easily manipulated by varying the applied potential. The H_2/CO ratios range from 4.2 to 0.28 in 4.3Pd-SnO_2 catalyst, when the applied potentials vary from − 0.5 to − 1.1 V. The H_2/CO ratio can effectively maintain under a long-term durability test of 30 h. Electrochemical test and theory calculations demonstrate that the formation of Pd-SnO_2 interface can lead the charge density redistribution of catalytic interfaces and change the energy-favorable intermediates adsorption from *OCHO in SnO_2 NSs to *COOH on Pd-SnO_2 NSs, thus improving the selectivity of CO with wide range of H_2/CO ratios for syngas production.

2. Experimental section

2.1. Chemicals and materials

Tin(IV) chloride pentahydrate ($SnCl_4 \cdot 5H_2O$), palladium(II) nitrate, ethylene glycol, ethanol, N-ethyl-4-piperidinecarboxamide hydrochloride, and potassium bicarbonate ($KHCO_3$) were bought from Sinopharm (Shanghai, China). Nafion solution, Nafion@117 film and nafion solution were obtained from Alfa Aesar.

2.2. Preparation of SnO_2 NSs

The procedure of the preparation of SnO_2 NSs is illustrated in Scheme 1. Firstly, graphene oxide (GO) nanosheets were fabricated by a typical method [42]. Then, the as-prepared GO nanosheets (15 mg) and $SnCl_4$ (0.75 mmol) were mixed in a 150 mL pH 2.2 buffer solution (2.07 g glycinesodium hydroxide and 462 mL ethylene glycol in an 88 mL H_2O and 2 mL HCl) and dispersed by ultrasound for 15 min. Subsequently, the mixture was vigorously stirred at 70 °C for 4 h to get the SnO_2-GO precursor. Finally, The SnO_2 NSs were obtained by calcining the SnO_2-GO precursor and removing the GO templates.

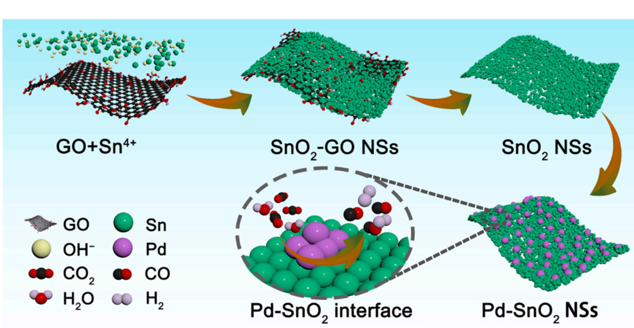

Scheme 1. Schematic illustration of the synthesis process of Pd-SnO_2 NSs.

2.3. Preparation of Pd-SnO_2 NSs

The different content of Pd-SnO_2 NSs were preparation by photodeposition method. Specifically, SnO_2 NSs (20 mg) were added in the mixed solution of ethyl alcohol (10 mL) and H_2O (100 mL) and treated with ultrasound for 15 min at room temperature. Then, Pd^{2+} aqueous solution with different concentrations was slowly added drop by drop under vigorously stirring for 30 min at dark conditions. Subsequently, the solution was transferred to a photocatalytic reaction chamber equipped with a 350 W xenon lamp and irradiated the suspension for 4 h under continuous agitation. The color of the suspension changed from yellow to dark gray, indicating that the Pd had been loaded on the surface of SnO_2 NSs. The gray powder after centrifugation of suspension was washed three times with deionized water and ethanol, respectively. Finally, the powder was dried overnight at 80 °C to get Pd-SnO_2 NSs.

2.4. Electrochemical measurements

The electrochemical measurements were performed in the CO_2-saturated 0.5 M $KHCO_3$ electrolyte with Nafion-membrane separated airtight H-type cell, where Ag/AgCl electrode and Pt electrode weres used as the reference electrode and counter electrode, respectively. The working electrode was prepared by immobilization of the electrocatalyst on carbon paper (1.5 cm × 0.5 cm). Typically, electrocatalyst (10 mg) and Nafion solution (50 μL 5 wt%) were dispersed in the mixed solution of 0.5 mL ethanol and 0.5 mL H_2O with sonicating for 20 min to form a homogeneous catalyst ink. Then, the catalyst ink (50 μL) was uniformly deposited on a piece of carbon paper (1.0 cm× 0.5 cm) to act as the working electrode. The potentials reported are all converted into reversible hydrogen electrode (RHE). $E(\mathrm{RHE}) = E(\mathrm{Ag/AgCl}) + 0.1989\ \mathrm{V} + 0.059 \times \mathrm{pH}$.

2.5. DFT models and calculations

The free energies of CO_2 reduction states were calculated by using codes from Vienna Ab-initio Simulation Package (VASP). The projector augmented wave (PAW) pseudopotential with the PBE generalized gradient approximation (GGA) exchange correlation function. For all the geometry optimizations, the cutoff energy of the plane waves basis set was 500 eV and a Monkhorst-Pack mesh of 3 × 3 × 1 was used in K-sampling in the adsorption energy calculation and 7 × 7 × 1 was used in K-sampling in the density of state (DOS) calculation. All atoms were fully relaxed with the energy convergence tolerance of 10 −5 eV per atom, and the final force on each atom was < 0.05 eV Å^{-1}. All periodic slabs have a vacuum layer of at least 15 Å. The bottom layer of atoms was fixed at their optimized bulk-truncated positions during geometry optimization, and the rest of atoms could relax. The adsorption energy of reaction intermediates can be calculated using the following equation:

$$\Delta E = E_{\mathrm{ads}} - E^{*},\ \Delta G = \Delta E + \Delta E_{\mathrm{ZPE}} - T\Delta S,$$

Where, ΔE_{ZPE} is the zero-point energy change, ΔS is the entropy change. In this work, the values of ΔE_{ZPE} and ΔS were obtained by vibration frequency calculation.

3. Results and discussion

3.1. Synthesis and characterizations of the catalysts

To characterize the structures of the as-prepared samples, the transmission electron microscopy (TEM) characterizations were carried out. As shown in Fig. 1a & b, SnO_2-GO NSs precursors possess large-size ultrathin morphology, like that of the GO NSs template. The sizes of SnO_2-GO NSs are about 3–5 μm. After calcining the SnO_2-GO precursor,

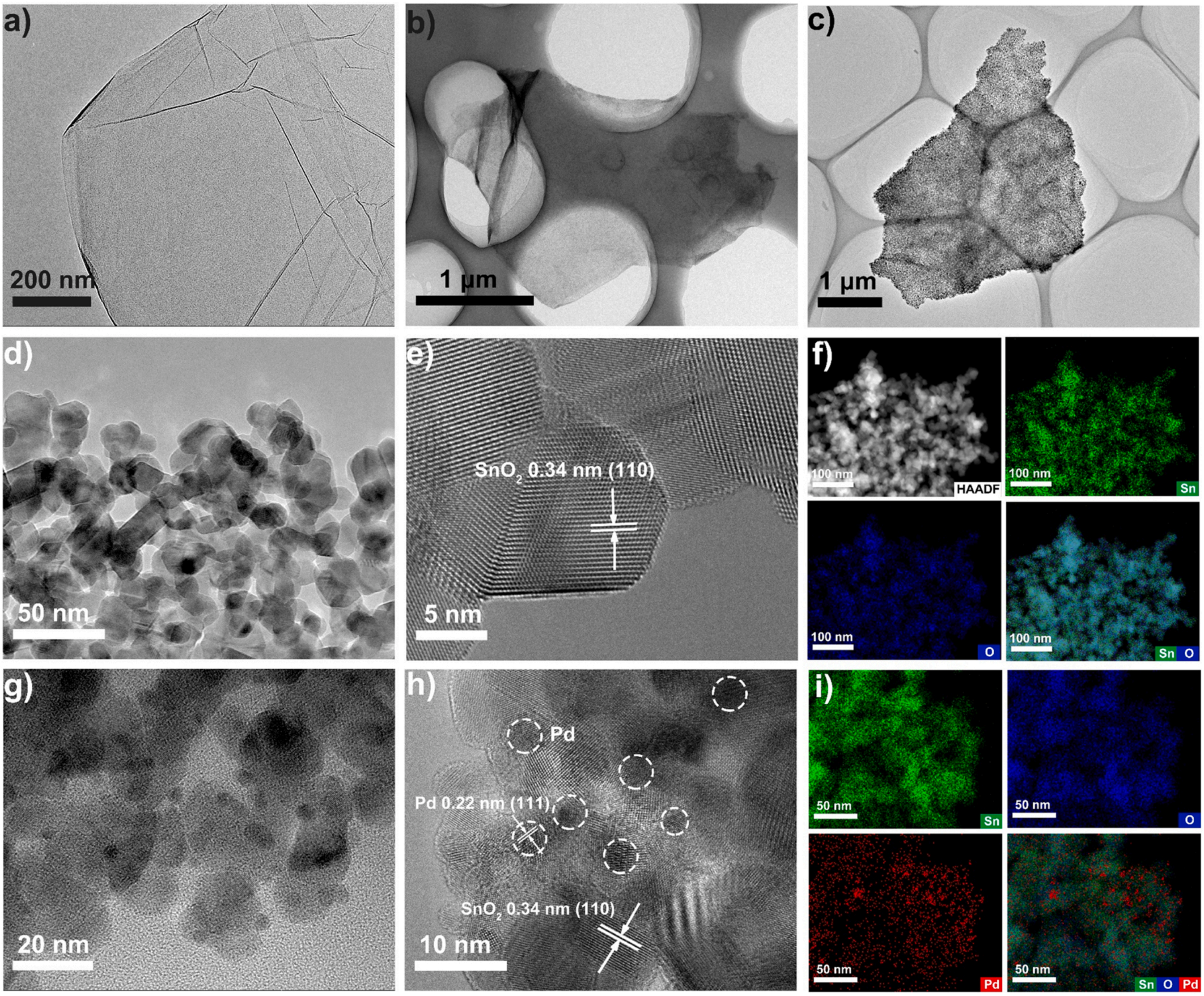

Fig. 1. Synthesis and structural characterization. TEM image of a) GO NSs, b) SnO_2-GO NSs, c) SnO_2 NSs. d) high-magnification TEM image, e) high-resolution TEM image and f) corresponding elemental mappings of SnO_2 NSs. g) TEM image, h) high-resolution TEM image and i) corresponding elemental mappings of Pd-SnO_2 NSs.

the GO NSs were removed, and the as-obtained SnO_2 NSs remain large-size two-dimensional structures (Fig. 1c & d). The high-resolution TEM (HR-TEM) image in Fig. 1e displays a clear interplanar spacing of 0.34 nm, ascribing to the (1 1 0) facet of the tetragonal SnO_2. Meanwhile, the high-angle annular darkfield scanning transmission electron microscopy (HAADF-STEM) analysis for SnO_2 NSs exhibit that Sn and O elements are distributed uniformly on the nanosheets (Fig. 1f). As shown in Fig. 1d, SnO_2 NSs are mainly composed of small SnO_2 particles, which leads to a rough surface, in favour of increasing the surface area. Thus, Pd can be anchored on the surface of SnO_2NSs via photo-deposition method. As shown in Fig. S1 and Fig. 1g, Pd-SnO_2 NSs possess also 2D large sizes morphology. The Pd nanoparticles with an average diameter of about 4 nm are uniformly attached on the surface of SnO_2 NSs. In comparison with SnO_2 NSs, Pd-SnO_2 NSs exhibits lattice fringes with a d-spacing of 0.34 and 0.22 nm (Fig. 1h), corresponding to the (110) facet of SnO_2 and the (111) plane of Pd, respectively. The successful loading of Pd into SnO_2 supports are also confirmed by the elemental mappings. Besides Sn and O elements, the uniform Pd element is observed in the corresponding elemental mappings of Pd-SnO_2 NSs (Fig. 1i).

To further elucidate the structural and chemical information of the Pd-SnO_2 NSs catalysts, inductively coupled plasma optical emission spectrometry (ICP-OES), X-ray diffraction (XRD) and Raman spectroscopy were preformed. The Pd-SnO_2 catalysts are denoted as xPd-SnO_2 (x: weight percentage of Pd in the catalyst). According to the ICP-OES analysis, the Pd contents in 2.2Pd-SnO_2, 4.3Pd-SnO_2 and 7.5Pd-SnO_2 catalysts are 2.2%, 4.3% and 7.5%, respectively. The crystalline structures of SnO_2 NSs and Pd-SnO_2 NSs are presented in Fig. 2a. SnO_2 NSs supports only exhibit the peaks of the SnO_2 crystalline lattice (JCPDS No. 41–1445). Meanwhile, no characteristic diffraction peaks of Pd or PdO were found in the XRD patterns of 2.2Pd-SnO_2 and 4.3Pd-SnO_2 catalyst, which can be attributed to the trace Pd loading beyond the detection limit of XRD [43,44]. When the Pd content increases to 7.5%, a weak characteristic peak of Pd is observed at 7.5% Pd-SnO_2 NSs, which is consistent with the Pd crystalline lattice (JCPDS No. 46–1043). Furthermore, the Raman spectroscopy of SnO_2 NSs exhibits three characteristic fingerprint peaks at 507.5, 633.2 and 773.7 cm^{-1}, corresponding to the three Raman active phonon modes: E_g, A_{1g} and B_{2g} of SnO_2 [45]. After the deposition of Pd on the SnO_2 surface, all Raman active phonon modes of SnO_2 obviously shift to the lower wavelength. This is attributed to the surface plasmon resonance from Pd-modification on SnO_2 surface, indicating that specific electromagnetic interact exists in the Pd metal and SnO_2 semiconductor surface.

The composition analysis was conducted by X-ray photoelectron spectroscopy (XPS), which were calibrated via its C1s reference value of

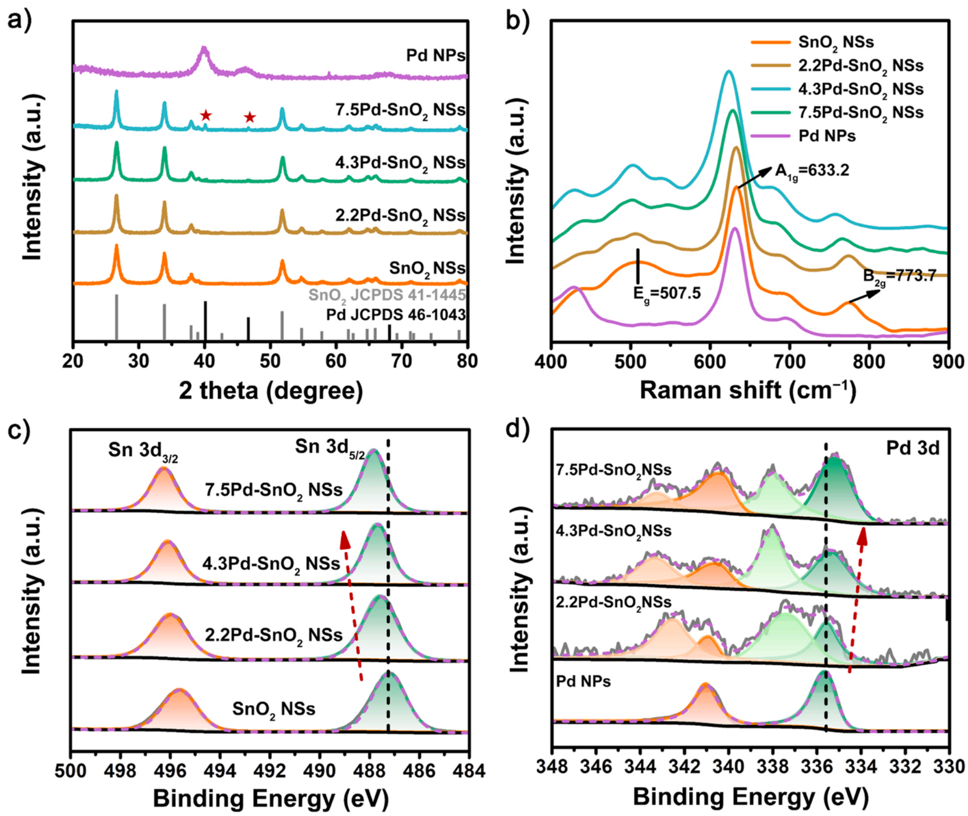

Fig. 2. a) XRD spectra and b) Raman spectroscopy of SnO_2 NSs, Pd-SnO_2 NSs and Pd NPs. c) Sn 3d XPS spectra of SnO_2 NSs, and Pd-SnO_2 NSs. d) Pd 3d XPS spectra of Pd NPs and Pd-SnO_2 NSs.

284 eV. The coexistence of Sn, O and Pd elements are clearly observed in the full-range XPS spectra for all Pd-SnO_2 NSs samples, comparing with that of the Pd free SnO_2 NSs sample (Fig. S2). Moreover, the high-resolution spectra of Sn 3d in Fig. S3 show that the two main peaks (495.61 and 487.18 eV in SnO_2 NSs, 495.95 and 487.54 eV in 2.2Pd-SnO_2 NSs, 496.06 and 487.68 eV in 4.3Pd-SnO_2 NSs, 496.29 and 487.79 eV in 7.5Pd-SnO_2 NSs), which can be assigned to the characteristic spin-orbit split Sn $3d_{3/2}$ and $3d_{5/2}$ oxidation state of SnO_2 [31]. Remarkably, the two peaks of Sn 3d shift to high binding energy with the increase of Pd content, indicating strong interaction and electron transfer in Pd-SnO_2 interface, due to the higher electronegativity of Pd than Sn. In the Pd 3d spectra of Pd NPs (Fig. S4), the $3d_{5/2}$ and $3d_{3/2}$ peak located at 335.09 and 340.45 eV are the characteristic of metallic Pd^0. After the formation of Pd-SnO_2 interface, the two 3d peaks of Pd^0 shift to lower binding energy, implying an electron-rich state (Fig. 2d). Meanwhile, the Pd 3d spectra of Pd-SnO_2 NSs can fit with two components, in which the other two peaks are assigned to Pd(II) in the Pd−O state. The high-resolution O 1 S XPS spectra of SnO_2 NSs exhibits two peaks at 532.08 and 531.09 eV, representing the O 1 s peaks for O−H and O−Sn (Fig. S5). And a weak additional O−Pd peak at 533.36 eV are observed at Pd-SnO_2 NSs, confirming the successful immobilization of Pd on SnO_2 surface and the formation of Pd−O−Sn interaction. The above results demonstrate that the formation of Pd-SnO_2 interface promotes the strong electron transfer between Sn and Pd, and generates electron-rich state sites, which is helpful to coupling the electron-deficient *COOH intermediates, thus enhancing the CO selectivity [46].

3.2. Electrocatalytic CO_2 reduction performance of the catalysts

The electrocatalytic performance of Pd-SnO_2 NSs for production of syngas was evaluated using Pd-SnO_2 NSs catalyst-modified carbon paper as a working electrode in a CO_2-saturated 0.5 M $KHCO_3$ aqueous solution. Linear sweep voltammetry (LSV) measurements are performed at scan rate of 50 mV s^{-1}. It shows that SnO_2 NSs, Pd-SnO_2 NSs and Pd NPs catalysts exhibit higher current density in CO_2-saturated than that in a N_2-saturated aqueous solution, suggesting effective eCO_2RR catalytic activity (Fig. S6). Significantly, the current densities in both CO_2-saturated and N_2-saturated solution increase gradually with the increase of the Pd content, suggesting that the Pd-SnO_2 interface can boost eCO_2RR and HER and be favour of producing syngas (Fig. 3a). Moreover, the increase of the Pd content effectively reduce the overpotential of Pd-SnO_2 NSs, ascribing to the improved conductivity of the catalyst with the addition of Pd.

As shown in Fig. 3b, CO, HCOOH and H_2 are found in the products on SnO_2 NSs catalyst, where the Faraday efficiency (FE) of HCOOH reaches 22.8% – 51.5%. Such high production of HCOOH needs to consume a large amount of electricity, resulting in low energy efficiency and diminished selectivity for the target syngas. In contrast, only CO and H_2, but no HCOOH produced upon Pd NPs. However, the proportion of CO is less than 10% at the applied potential, which is not suitable for the practical application (Fig. 3c). It is worthwhile to note that the *FE* of HCOOH gradually decreases with the increasing of the Pd content of Pd-SnO_2 (i.e., increasing the interface area of the catalyst). For example, upon 2.2Pd-SnO_2 NSs catalyst, the *FE* of HCOOH drops below 15.7% (Fig. 3d); while the total FE for CO + H_2 on 4.3Pd-SnO_2 catalyst and 7.5Pd-SnO_2 NSs reaches close to 100% (Fig. 3e & f). When the potential sweeps from − 0.5 to − 1.1 V, the FE_{CO} on 4.3Pd-SnO_2 catalyst gradually increased to a maximum of 78.6% at − 0.9 V (H_2/CO ratio: 0.28); afterwards, the FE_{CO} decreased, similar trend was observed on 7.5Pd-SnO_2 NSs. Distinctly, the maximum of FE_{CO} on 7.5Pd-SnO_2 NSs is only 65.8% (H_2/CO ratio: 0.52), which attributes to the fact that high Pd incorporation leads to a booting HER. As shown in Fig. 3g and Fig. S7, by adjusting applied potential (−0.5 to −1.1 V), the optimal 4.3Pd-SnO_2 catalyst exhibit a controllable H_2/CO ratio ranged from 4.2 to 0.28, which is wider than that of SnO_2 NSs (2.4–0.83), 2.2Pd-SnO_2 NSs

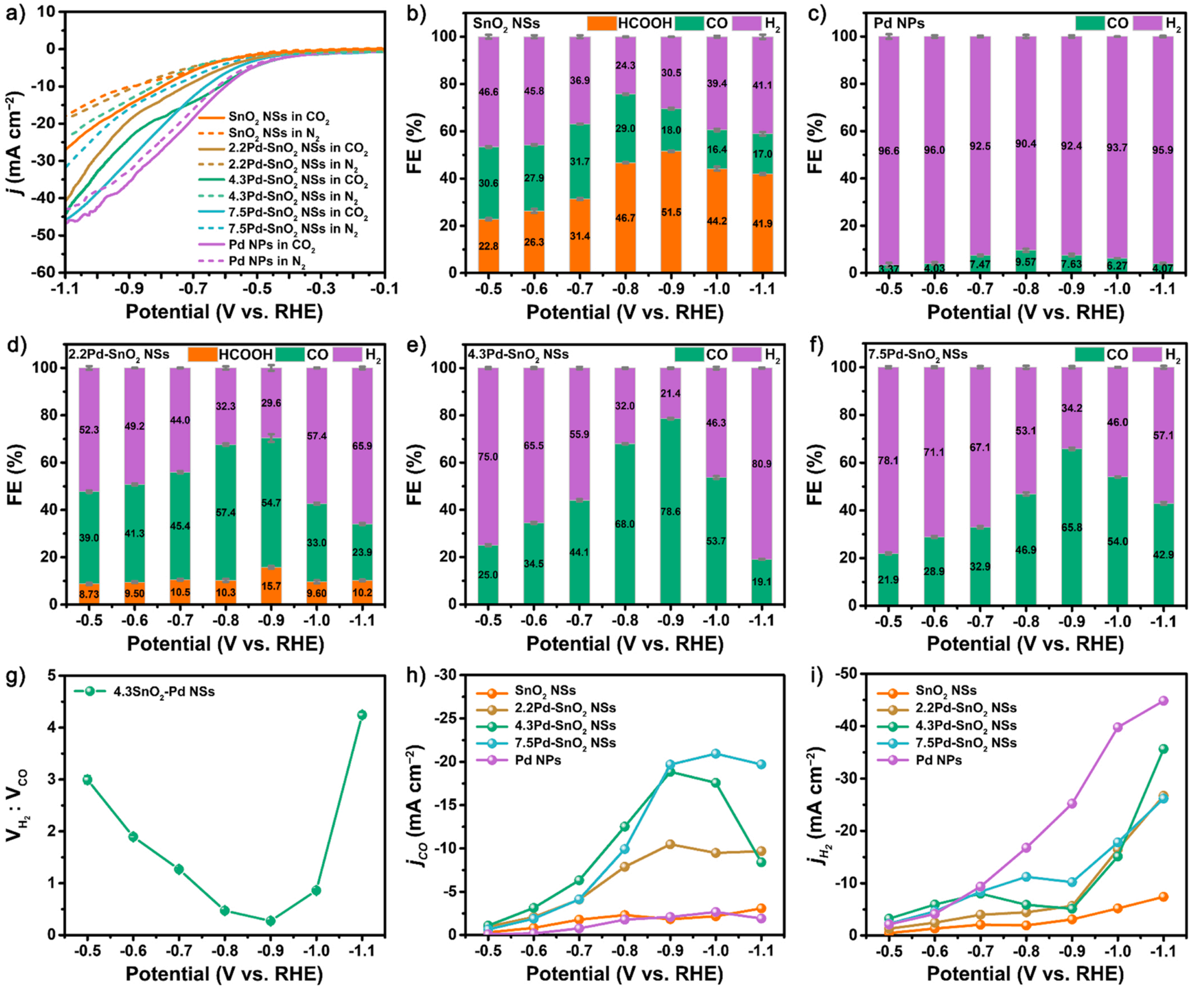

Fig. 3. a) LSV curves of SnO_2 NSs, Pd-SnO_2 NSs and Pd NPs. FE on b) SnO_2 NSs, c) Pd NPs, d) 2.2Pd-SnO_2 NSs, e) 4.3Pd-SnO_2 NSs and f) 7.5Pd-SnO_2 NSs. g) Volume ratio between H_2 and CO vs. the applied potential on 4.3 Pd-SnO_2 NSs. h) CO and i) H_2 partial current density on SnO_2 NSs, Pd-SnO_2 NSs and Pd NPs. The products at the applied potential (−0.5 to −1.1 V) are collected and quantified by ^{1}H NMR and gas chromatography (GC).

(2.7–0.54), 7.5Pd-SnO_2 NSs (3.5–0.51) and Pd NP. Notably, the HCOOH production on 4.3Pd-SnO_2 catalyst and 7.5Pd-SnO_2 NSs catalyst is completely inhibited. As illustrated in Fig. 3h and i, Pd-SnO_2 NSs possess higher j_{CO} and j_{H2} than that of SnO_2 NSs, indicating the high activity of eCO_2RR and HER after the formation of Pd-SnO_2 interface. Though 7.5Pd-SnO_2 NSs catalyst displays the highest j_{CO} at high current density range, 4.3Pd-SnO_2 catalyst shows larger range of CO/H_2 ratio at the applied potentials, which is apt to control the H_2/CO ratio. The HCOOH partial current density show that the eCO_2RR to HCOOH pathway is suppressed on Pd-SnO_2 NSs (Fig. S8).

To gain insight into the kinetics of eCO_2RR on the Pd-SnO_2 interface, Tafel analysis and electrochemical impedance spectroscopy (EIS) were investigated. As presented in Fig. 4a, 4.3Pd-SnO_2 NSs exhibit the lowest Tafel slope (128 mV dec^{-1}) compared with those of SnO_2 NSs (165 mV dec^{-1}), 2.2Pd-SnO_2 (143 mV dec^{-1}) and 7.5Pd-SnO_2 NSs (136 mV dec^{-1}). Fig. 4b shows that Pd-SnO_2 NSs possess the smaller radius than SnO_2 NSs, suggesting the lower charge transfer resistance, which is contributed to the immobilization of Pd on the surface of SnO_2 NSs. These results confirm that the formation of Pd-SnO_2 interface can improve the activity of eCO_2RR to CO. In addition, the stability of 4.3Pd-SnO_2 NSs was measured at a long-time electrolysis under potential of − 0.6 or − 0.9 V. Clearly, both FE_{CO} and FE_{H2} kept constant for 30 h (Fig. 4c). The morphology and valance of 4.3Pd-SnO_2 NSs after electrolysis was characterized by TEM, XRD and XPS. As shown in Fig. S9, no obvious changes in the structures of 4.3Pd-SnO_2 NSs after electrolysis, suggesting that the catalyst is of high stability. In addition, eCO_2RR performance of 4.3Pd-SnO_2 NSs are evaluated using the flow cell. As shown in Fig. S10, the eCO_2RR to HCOOH pathway of 4.3Pd-SnO_2 NSs is still suppressed at high current density (>100 mA cm^{-2}). The optimal 4.3Pd-SnO_2 NSs exhibit controllable H_2/CO ratios ranged from 9.2 to 0.26.

3.3. Experimental and theoretical study of the catalytic mechanism of Pd-SnO_2 Interface

To clarify the reaction pathways of the catalysts, in-situ ATR-FTIR spectra of the catalyst at different applied potentials were carried out. The peaks at 1542 and 1646 cm^{-1} assigned to the characteristic peaks of *CO_2^- intermediates, are increasingly apparent on SnO_2 NSs and 4.3Pd-SnO_2 NSs surface (Fig. 4d & e) than that on Pd NPs surface (Fig. 4f), indicating a higher eCO_2RR activity of SnO_2 NSs and 4.3Pd-SnO_2 NSs than that of Pd [47,48]. When the applied potential was below − 0.5 V,

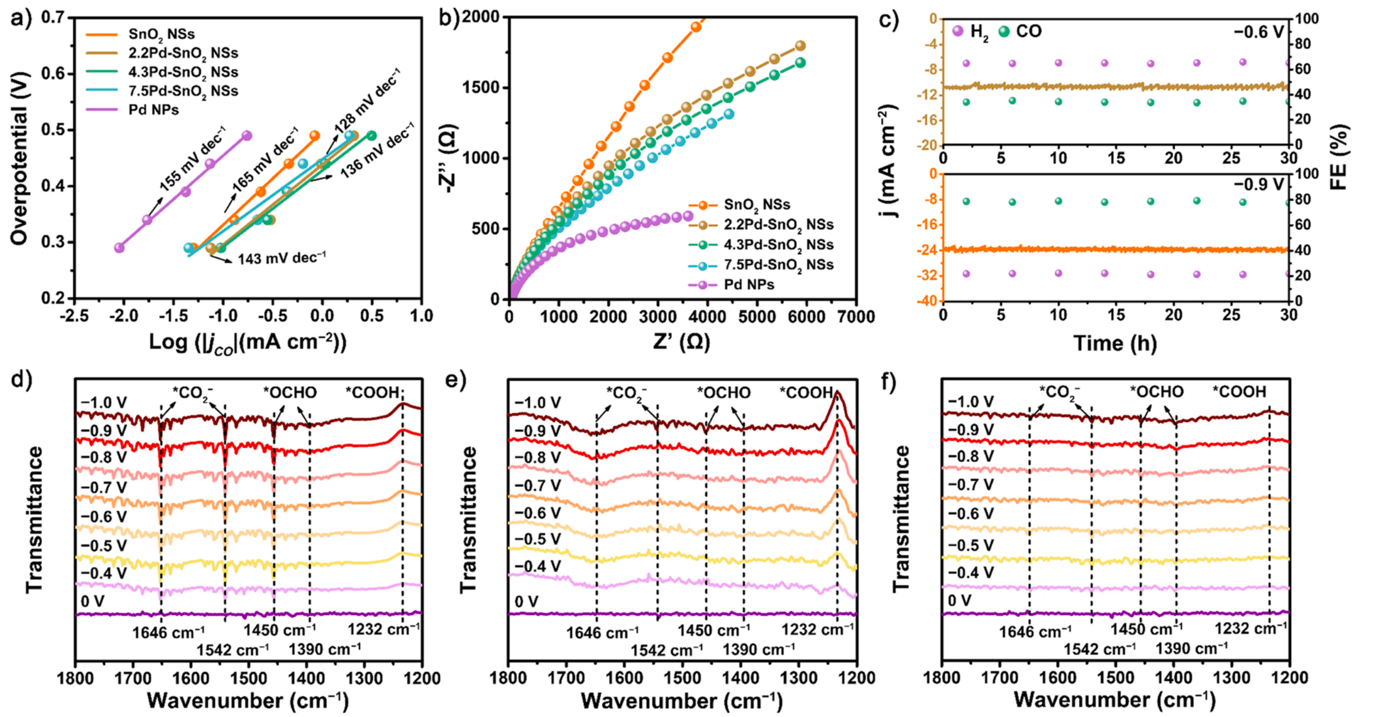

Fig. 4. a) Tafel analysis and b) electrochemical impedance spectroscopy (EIS) of SnO_2 NSs, Pd-SnO_2 NSs and Pd NPs. c) the stability test for 4.3Pd-SnO_2 NSs at − 0.6 and − 0.9 eV. In situ ATR-FTIR spectra of d) SnO_2 NSs, e) 4.3Pd-SnO_2 NSs and f) Pd NPs.

the strengthened vibrational band of *COOH species at 1232 cm^{-1} appears clearly on 4.3Pd-SnO_2 NSs, but no distinguish peaks can be observed on the surface of SnO_2 NSs or Pd NPs, which demonstrates that the interface of Pd-SnO_2 possesses high ability to stabilization of the key *COOH intermediates, subsequently promoting the CO pathway. Furthermore, the peaks centered about 1390 and 1450 cm^{-1} assigned to *OCHO species is the key intermediate for HCOOH formation [49,50]. These peaks are not observed on 4.3Pd-SnO_2 NSs and Pd NPs catalysts, confirming that the cooperation of Pd with SnO_2 can effectively inhibit the generation of HCOOH. Meanwhile, three catalysts show no typical peaks *CO located at 1900 – 2100 cm^{-1}, suggesting no C_{2+} products pathways (Fig. S11). Consequently, the active Pd-SnO_2 interface can

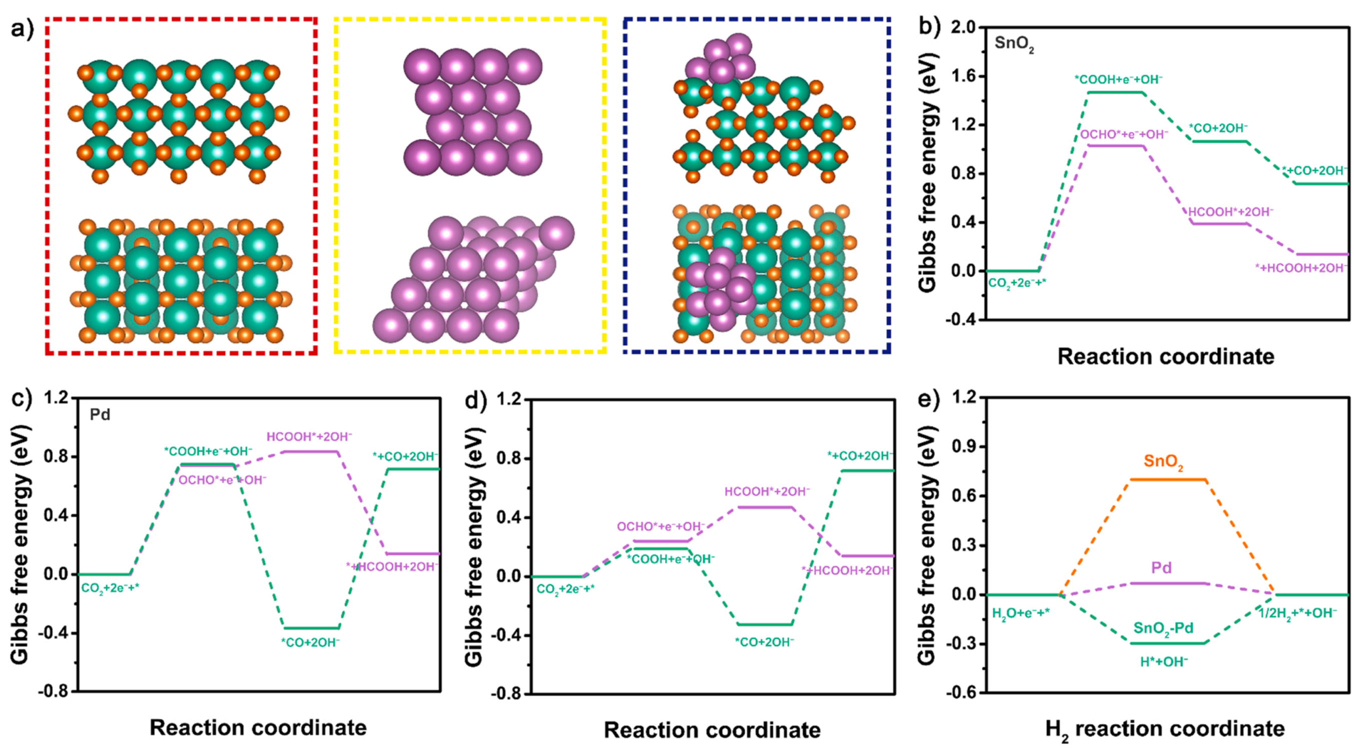

Fig. 5. a) Calculated crystal structure of SnO_2 (red dotted box), Pd (yellow dotted box), and SnO_2-Pd (blue dotted box). The Gibbs free energies of HCCOH and CO reaction coordinate for b) SnO_2, c) Pd and d) Pd-SnO_2. e) The Gibbs free energies H_2 reaction coordinate.

accelerate the intermediates formation of *COOH, while suppress *OCHO species, thus enhancing the efficiency of syngas production.

To gain insight into the effects of Pd-SnO_2 interface on the thermochemical reaction energy and the adsorption behavior of the key intermediates, density-functional theory (DFT) analysis was performed in the surface-load-type Pd-SnO_2 interface. The models are shown in Fig. 5a. The optimized structures of the reactants and intermediates (*COOH, *CO, *OCHO, HCOOH* and H*) on SnO_2, Pd and Pd-SnO_2 models are shown in Figs. S12–S14, respectively. For the eCO_2RR to CO pathway, Pd-SnO_2 catalyst reveals the energy-favourable trend compared to SnO_2 and Pd (Fig. S15). Specifically, the Δ. for the formation of *COOH (the key intermediate for CO) on Pd-SnO_2 is 0.19 eV, which is lower than that on SnO_2 (1.47 eV) and Pd (0.75 eV) suggesting that Pd-SnO_2 interface can facilitate CO production. For HCOOH production, the Δa for the formation of *OCHO reduce to 0.24 eV from SnO_2 (1.03 eV) and Pd (0.75 eV). However, the Δ of *HCOOH on Pd-SnO_2 (0.48 eV) is higher than that on SnO_2 (0.38 eV). Therefore, the dominant reaction pathway varies on three models. On the SnO_2 surface, the Δt for the formation of *OCHO and HCOOH* are lower than *COOH and *CO (Fig. 5b), resulting in the ascendant HCOOH production. In converse, on Pd and Pd-SnO_2 surface, the CO pathway is more preponderant on Pd and Pd-SnO_2 as shown in Fig. 5c & d. For the HER pathway (Fig. 5e), the Δh for the formation of *H on Pd-SnO_2 (−0.30 eV) is more favourable that SnO_2 (0.70 eV). Consequently, the HER reaction is facilitated on Pd-SnO_2 interface. Therefore, the theoretical results suggest that the Pd-SnO_2 interface could regulate the adsorption and desorption behavior of intermediates, and boost syngas production.

4. Conclusion

In summary, we establish Pd-SnO_2 catalysts for eCO_2RR to syngas. The catalysts show great potential to control the eCO_2RR and HRE processes, suppressing the HCOOH selectivity for efficient syngas production with controllable H_2/CO ratios. The optimal 4.3Pd-SnO_2 catalyst exhibit a competitive activity for CO and H_2 generation. The H_2/CO ratio can range from 4.2 to 0.28 by adjusting the applied potential. Moreover, the H_2/CO ratio can effectively maintain under a long-term durability test of 30 h. Electrochemical test and theory calculations demonstrate that with the formation and increasing of Pd-SnO_2 interface, the active Pd-SnO_2 interface accelerates the intermediates formation of *COOH, and suppresses HCOOH pathway, thus improving the selectivity of CO for controllable H_2/CO ratios of syngas production. This work unfolds a promising candidate for earth-abundant Sn-based electrocatalysts towards CO_2 electroreduction to syngas.

CRediT authorship contribution statement

Haichuan He: Conceptualization, Methodology, Investigation, Formal analysis, Visualization, Writing – original draft, Reviewing and editing. **Dan Xia**: Conceptualization, Validation, Formal analysis. **Xiao Yu:** Investigation, Visualization. **Jian Wu**: Data curation. **Yan Wang**: Data curation, Formal analysis. **Fei Chen**: Data curation, Investigation. **Dr. Liqiang Wang:** Data curation. **Dr. Linlin Wu:** Conceptualization. **Dr. Jianhan Huang:** Conceptualization, Methodology, Visualization. **Dr. Ning Zhao:** Methodology, Visualization. **Dr. Liu Deng**: Conceptualization, Methodology, Visualization, Writing – original draft, Writing – review & editing. **Dr. You-Nian Liu**: Corresponding author, Supervision, Conceptualization, Writing – original draft preparation, Reviewing and editing.

Declaration of Competing Interest

The authors declare that they have no known competing financial interests or personal relationships that could have appeared to influence the work reported in this paper.

Acknowledgements

This work was supported by the National Natural Science Foundation of China (Nos. 21636010, 21878342 and 22178393), the Foundation of State Key Laboratory of Coal Conversion, Shanxi, China (Grant No. J21–22-609), and the Hunan Provincial Science and Technology Plan Project, China (No. 2019TP1001 and 2020JJ3044).

Appendix A. Supporting information

Supplementary data associated with this article can be found in the online version at doi:10.1016/j.apcatb.2022.121392.

References

[1] S. Guo, S. Zhao, X. Wu, H. Li, Y. Zhou, C. Zhu, N. Yang, X. Jiang, J. Gao, L. Bai, Y. Liu, Y. Lifshitz, S.T. Lee, Z. Kang, A Co_3O_4-CDots-C_3N_4 three component electrocatalyst design concept for efficient and tunable CO_2 reduction to syngas (https://), Nat. Commun. 8 (2017) 1828, https://doi.org/10.1038/s41467-017-01893-7.

[2] R. Zhang, H. Wang, S. Tang, C. Liu, F. Dong, H. Yue, B. Liang, Photocatalytic oxidative dehydrogenation of ethane using CO_2 as a soft oxidant over Pd/TiO_2 catalysts to C_2H_4 and syngas (https://), ACS Catal. 8 (2018) 9280–9286, https://doi.org/10.1021/acscatal.8b02441.

[3] C. Li, T. Wang, B. Liu, M. Chen, A. Li, G. Zhang, M. Du, H. Wang, S.F. Liu, J. Gong, Photoelectrochemical CO_2 reduction to adjustable syngas on grain-boundary-mediated a-Si/TiO_2/Au photocathodes with low onset potentials (https://), Energy Environ. Sci. 12 (2019) 923–928, https://doi.org/10.1039/c8ee02768d.

[4] L. Zhong, F. Yu, Y. An, Y. Zhao, Y. Sun, Z. Li, T. Lin, Y. Lin, X. Qi, Y. Dai, L. Gu, J. Hu, S. Jin, Q. Shen, H. Wang, Cobalt carbide nanoprisms for direct production of lower olefins from syngas (https://), Nature 538 (2016) 84–87, https://doi.org/10.1038/nature19786.

[5] H. He, J. Wu, X. Yu, D. Xia, Y. Wang, F. Chen, L. Wang, L. Wu, J. Huang, N. Zhao, L. Deng, Y.-N. Liu, Dual-active sites design of Sn_x-Sb_y-O-GO nanosheets for enhancing electrochemical CO_2 reduction via Sb-accelerating water activation (https://), Appl. Catal. B Environ. 307 (2022), 121171, https://doi.org/10.1016/j.apcatb.2022.121171.

[6] J. Kopyscinski, T.J. Schildhauer, S.M.A. Biollaz, Production of synthetic natural gas (SNG) from coal and dry biomass – A technology review from 1950 to 2009 (https://), Fuel 89 (2010) 1763–1783, https://doi.org/10.1016/j.fuel.2010.01.027.

[7] S. Li, X. Ji, X. Zhang, L. Gao, H. Jin, Coal to SNG: technical progress, modeling and system optimization through exergy analysis (https://), Appl. Energy 136 (2014) 98–109, https://doi.org/10.1016/j.apenergy.2014.09.006.

[8] J. Witte, A. Kunz, S.M.A. Biollaz, T.J. Schildhauer, Direct catalytic methanation of biogas – Part II: techno-economic process assessment and feasibility reflections (https://), Energy Convers. Manag. 178 (2018) 26–43, https://doi.org/10.1016/j.enconman.2018.09.079.

[9] G. Zhang, T. Sun, J. Peng, S. Wang, S. Wang, A comparison of Ni/SiC and Ni/Al_2O_3 catalyzed total methanation for production of synthetic natural gas (https://), Appl. Catal. A Gen. 462 (2013) 75–81, https://doi.org/10.1016/j.apcata.2013.04.037.

[10] W. Ren, X. Tan, J. Qu, S. Li, J. Li, X. Liu, S.P. Ringer, J.M. Cairney, K. Wang, S. C. Smith, C. Zhao, Isolated copper-tin atomic interfaces tuning electrocatalytic CO_2 conversion (https://), Nat. Commun. 12 (2021) 1449, https://doi.org/10.1038/s41467-021-21750-y.

[11] J. Pei, T. Wang, R. Sui, X. Zhang, D. Zhou, F. Qin, X. Zhao, Q. Liu, W. Yan, J. Dong, L. Zheng, A. Li, J. Mao, W. Zhu, W. Chen, Z. Zhuang, N-Bridged Co–N–Ni: new bimetallic sites for promoting electrochemical CO_2 reduction (https://), Energy Environ. Sci. 14 (2021) 3019–3028, https://doi.org/10.1039/d0ee03947k.

[12] Z. Zhang, G. Wen, D. Luo, B. Ren, Y. Zhu, R. Gao, H. Dou, G. Sun, M. Feng, Z. Bai, A. Yu, Z. Chen, "Two ships in a bottle" design for Zn-Ag-O catalyst enabling selective and long-lasting CO_2 electroreduction (https://), J. Am. Chem. Soc. 143 (2021) 6855–6864, https://doi.org/10.1021/jacs.0c12418.

[13] G. Wen, B. Ren, M.G. Park, J. Yang, H. Dou, Z. Zhang, Y.P. Deng, Z. Bai, L. Yang, J. Gostick, G.A. Botton, Y. Hu, Z. Chen, Ternary Sn-Ti-O elctrocatalyst boosts the stability and energy efficiency of CO_2 reduction (https://), Angew. Chem. Int. Ed. 59 (2020) 12860–12867, https://doi.org/10.1002/anie.202004149.

[14] H. Park, J. Choi, H. Kim, E. Hwang, D.-H. Ha, S.H. Ahn, S.-K. Kim, AgIn dendrite catalysts for electrochemical reduction of CO_2 to CO (https://), Appl. Catal. B Environ. 219 (2017) 123–131, https://doi.org/10.1016/j.apcatb.2017.07.038.

[15] Y.S. Ham, S. Choe, M.J. Kim, T. Lim, S.-K. Kim, J.J. Kim, Electrodeposited Ag catalysts for the electrochemical reduction of CO_2 to CO (https://), Appl. Catal. B Environ. 208 (2017) 35–43, https://doi.org/10.1016/j.apcatb.2017.02.040.

[16] R. Cui, Q. Shen, C. Guo, B. Tang, N. Yang, G. Zhao, Syngas electrosynthesis using self-supplied CO_2 from photoelectrocatalytic pollutant degradation (https://), Appl. Catal. B Environ. 261 (2020), https://doi.org/10.1016/j.apcatb.2019.118253.

[17] X.-Y. Zhang, J.-Y. Xie, Y. Ma, B. Dong, C.-G. Liu, Y.-M. Chai, Catalytic mechanisms and practical activity of the active site in transition metal electrocatalysts for hydrogen evolution reaction (https://), Chem. Eng. J. 430 (2021), 132312, https://doi.org/10.1016/j.cej.2021.132312.

[18] C. Wang, Y. Li, C. Gu, L. Zhang, X. Wang, J. Tu, Active Co@CoO core/shell nanowire arrays as efficient electrocatalysts for hydrogen evolution reaction (https://), Chem. Eng. J. 429 (2022), 132226, https://doi.org/10.1016/j.cej.2021.132226.

[19] H. Cheng, Y. Diao, Q. Liu, L. Wei, X. Li, J. Chen, F. Wang, Di-nuclear metal synergistic catalysis: $Ni_2Mo_6S_6O_2/MoS_2$ two-dimensional nanosheets for hydrogen evolution reaction (https://), Chem. Eng. J. 428 (2022), 131084, https://doi.org/10.1016/j.cej.2021.131084.

[20] Y. Yang, Y. Yu, J. Li, Q. Chen, Y. Du, P. Rao, R. Li, C. Jia, Z. Kang, P. Deng, Y. Shen, X. Tian, Engineering ruthenium-based electrocatalysts for effective hydrogen evolution reaction (https://), Nano-Micro Lett. 13 (2021) 160, https://doi.org/10.1007/s40820-021-00679-3.

[21] J. Yin, Q. Fan, Y. Li, F. Cheng, P. Zhou, P. Xi, S. Sun, Ni-C-N nanosheets as catalyst for hydrogen evolution reaction (https://), J. Am. Chem. Soc. 138 (2016) 14546–14549, https://doi.org/10.1021/jacs.6b09351.

[22] H. He, C. Yang, L. Deng, J. Wu, F. Chen, J. Huang, Y.-N. Liu, Inside-mode indium oxide/carbon nanotubes for efficient carbon dioxide electroreduction by suppressing hydrogen evolution (https://), Chem. Commun. 57 (2021) 1234–1237, https://doi.org/10.1039/d0cc07417a.

[23] D. Yang, Q. Zhu, X. Sun, C. Chen, W. Guo, G. Yang, B. Han, Electrosynthesis of a defective indium selenide with 3D structure on a substrate for tunable CO_2 electroreduction to syngas (https://), Angew. Chem. Int. Ed. 59 (2020) 2354–2359, https://doi.org/10.1002/anie.201914831.

[24] Y. Wang, C. Niu, Y. Zhu, D. He, W. Huang, Tunable syngas formation from electrochemical CO_2 reduction on copper nanowire arrays (https://), ACS Appl. Energy Mater. 3 (2020) 9841–9847, https://doi.org/10.1021/acsaem.0c01504.

[25] Q. He, D. Liu, J.H. Lee, Y. Liu, Z. Xie, S. Hwang, S. Kattel, L. Song, J.G. Chen, Electrochemical conversion of CO_2 to syngas with controllable CO/H_2 ratios over Co and Ni single-atom catalysts (https://), Angew. Chem. Int. Ed. 59 (2020) 3033–3037, https://doi.org/10.1002/anie.201912719.

[26] H. Chen, Z. Li, Z. Zhang, K. Jie, J. Li, H. Li, S. Mao, D. Wang, X. Lu, J. Fu, Synthesis of composition-tunable syngas from efficiently electrochemical conversion of CO_2 over AuCu/CNT bimetallic catalyst (https://), Ind. Eng. Chem. Res. 58 (2019) 15425–15431, https://doi.org/10.1021/acs.iecr.9b02192.

[27] M.-N. Zhu, B.-W. Zhang, M.-R. Gao, P.-F. Sui, C. Xu, L. Gong, H. Zeng, K. Shankar, S. Bergens, J.-L. Luo, Electrochemically reconstructed perovskite with cooperative catalytic sites for CO_2-to-formate conversion (https://), Appl. Catal. B Environ. 306 (2022), 121101, https://doi.org/10.1016/j.apcatb.2022.121101.

[28] J. Zeng, M.R. Fiorentin, M. Fontana, M. Castellino, F. Risplendi, A. Sacco, G. Cicero, M.A. Farkhondehfal, F. Drago, C.F. Pirri, Novel insights into Sb-Cu catalysts for electrochemical reduction of CO_2 (https://), Appl. Catal. B Environ. 306 (2022), 121089, https://doi.org/10.1016/j.apcatb.2022.121089.

[29] Y. Li, G. Shi, T. Chen, L. Zhu, D. Yu, Y. Sun, F. Besenbacher, M. Yu, Simultaneous increase of conductivity, active sites and structural strain by nitrogen injection for high-yield CO_2 electro-hydrogenation to liquid fuel (https://), Appl. Catal. B Environ. 305 (2022), 121080, https://doi.org/10.1016/j.apcatb.2022.121080.

[30] K. Chen, M. Cao, G. Ni, S. Chen, H. Liao, L. Zhu, H. Li, J. Fu, J. Hu, E. Cortés, M. Liu, Nickel polyphthalocyanine with electronic localization at the nickel site for enhanced CO_2 reduction reaction (https://), Appl. Catal. B Environ. 306 (2022), 121093, https://doi.org/10.1016/j.apcatb.2022.121093.

[31] H. He, K. Liu, K. Liang, A. Mustapha, Z. Wang, L. Wu, C. Yang, L. Deng, S. Guo, Y.-N. Liu, Boosting carbon dioxide electroreduction to C_1 feedstocks via theory-guided tailoring oxygen defects in porous tin-oxide nanocubes (https://), J. Catal. 385 (2020) 246–254, https://doi.org/10.1016/j.jcat.2020.03.015.

[32] K. Xu, S. Liu, Z. Cao, Y. Mao, Q. Mao, Pore-structure-enhanced electrochemical reduction of CO_2 to formate on Sn-based double-layer catalysts (https://), Electrochem. Commun. 128 (2021), 107056, https://doi.org/10.1016/j.elecom.2021.107056.

[33] B. Zhang, S. Chen, B. Wulan, J. Zhang, Surface modification of SnO_2 nanosheets via ultrathin N-doped carbon layers for improving CO_2 electrocatalytic reduction (https://), Chem. Eng. J. 421 (2021), 130003, https://doi.org/10.1016/j.cej.2021.130003.

[34] J. Liu, J. Zhao, X. Deng, Y. Sun, S. Imhanria, W. Wang, Sn and N co-doped porous carbon catalyst electrochemically reduce CO_2 into tunable syngas (https://), J. Taiwan Inst. Chem. E 121 (2021) 122–127, https://doi.org/10.1016/j.jtice.2021.03.039.

[35] M. Zhang, Z. Zhang, Z. Zhao, H. Huang, D.H. Anjum, D. Wang, J.-h He, K.-W. Huang, Tunable selectivity for electrochemical CO_2 reduction by bimetallic Cu–Sn catalysts: elucidating the roles of Cu and Sn (https://), ACS Catal. 11 (2021) 11103–11108, https://doi.org/10.1021/acscatal.1c02556.

[36] W. Zhang, Q. Qin, L. Dai, R. Qin, X. Zhao, X. Chen, D. Ou, J. Chen, T.T. Chuong, B. Wu, N. Zheng, Electrochemical reduction of carbon dioxide to methanol on hierarchical Pd/SnO_2 nanosheets with abundant Pd-O-Sn interfaces (https://), Angew. Chem. Int. Ed. 57 (2018) 9475–9479, https://doi.org/10.1002/anie.201804142.

[37] C. Xie, Z. Niu, D. Kim, M. Li, P. Yang, Surface and interface control in nanoparticle catalysis (https://), Chem. Rev. 120 (2020) 1184–1249, https://doi.org/10.1021/acs.chemrev.9b00220.

[38] G. Wen, D.U. Lee, B. Ren, F.M. Hassan, G. Jiang, Z.P. Cano, J. Gostick, E. Croiset, Z. Bai, L. Yang, Z. Chen, Orbital interactions in Bi-Sn bimetallic electrocatalysts for highly selective electrochemical CO_2 reduction toward formate production (https://), Adv. Energy Mater. 8 (2018), 1802427, https://doi.org/10.1002/aenm.201802427.

[39] W. Luo, W. Xie, R. Mutschler, E. Oveisi, G.L. De Gregorio, R. Buonsanti, A. Züttel, Selective and stable electroreduction of CO_2 to CO at the copper/indium interface (https://), ACS Catal. 8 (2018) 6571–6581, https://doi.org/10.1021/acscatal.7b04457.

[40] X. Zhao, X. Li, D. Xiao, M. Gong, L. An, P. Gao, J. Yang, D. Wang, Isolated Pd atom anchoring endows cobalt diselenides with regulated water-reduction kinetics for alkaline hydrogen evolution (https://), Appl. Catal. B Environ. 295 (2021), 120280, https://doi.org/10.1016/j.apcatb.2021.120280.

[41] H. Liao, C. Wei, J. Wang, A. Fisher, T. Sritharan, Z. Feng, Z.J. Xu, A multisite strategy for enhancing the hydrogen evolution reaction on a nano-Pd surface in alkaline media (https://), Adv. Energy Mater. 7 (2017), 1701129, https://doi.org/10.1002/aenm.201701129.

[42] H. Zhao, Y. Zhu, F. Li, R. Hao, S. Wang, L. Guo, A generalized strategy for the synthesis of large-size ultrathin two-dimensional metal oxide nanosheets (https://), Angew. Chem. Int. Ed. 56 (2017) 8766–8770, https://doi.org/10.1002/anie.201703871.

[43] N. Rui, Z. Wang, K. Sun, J. Ye, Q. Ge, C.-j Liu, CO_2 hydrogenation to methanol over Pd/In2O3: effects of Pd and oxygen vacancy (https://), Appl. Catal. B Environ. 218 (2017) 488–497, https://doi.org/10.1016/j.apcatb.2017.06.069.

[44] W. Wang, Z. Wang, M. Yang, C.-J. Zhong, C.-J. Liu, Highly active and stable Pt (111) catalysts synthesized by peptide assisted room temperature electron reduction for oxygen reduction reaction (https://), Nano Energy 25 (2016) 26–33, https://doi.org/10.1016/j.nanoen.2016.04.022.

[45] K. McGuire, Z.W. Pan, Z.L. Wang, D. Milkie, J. Menéndez, A.M. Rao, Raman studies of semiconducting oxide nanobelts (https://), J. Nanosci. Nanotech. 2 (2002) 499–502, https://doi.org/10.1166/jnn.2002.129.

[46] Y. Qiu, J. Zhang, J. Jin, J. Sun, H. Tang, Q. Chen, Z. Zhang, W. Sun, G. Meng, Q. Xu, Y. Zhu, A. Han, L. Gu, D. Wang, Y. Li, Construction of Pd-Zn dual sites to enhance the performance for ethanol electro-oxidation reaction (https://), Nat. Commun. 12 (2021) 5273, https://doi.org/10.1038/s41467-021-25600-9.

[47] J. Sheng, Y. He, J. Li, C. Yuan, H. Huang, S. Wang, Y. Sun, Z. Wang, F. Dong, Identification of halogen-associated active sites on bismuth-based perovskite quantum dots for efficient and selective CO_2-to-CO photoreduction (https://), ACS Nano 14 (2020) 13103–13114, https://doi.org/10.1021/acsnano.0c04659.

[48] H. Liu, J. Xia, N. Zhang, H. Cheng, W. Bi, X. Zu, W. Chu, H. Wu, C. Wu, Y. Xie, Solid–liquid phase transition induced electrocatalytic switching from hydrogen evolution to highly selective CO_2 reduction (https://), Nat. Catal. 4 (2021) 202–211, https://doi.org/10.1038/s41929-021-00576-3.

[49] Z. Wu, H. Wu, W. Cai, Z. Wen, B. Jia, L. Wang, W. Jin, T. Ma, Engineering bismuth-tin interface in bimetallic aerogel with a 3D porous structure for highly selective electrocatalytic $CO\text{-}_2$ reduction to HCOOH (https://), Angew. Chem. Int. Ed. 60 (2021) 12554–12559, https://doi.org/10.1002/anie.202102832.

[50] Y. Cheng, J. Hou, P. Kang, Integrated capture and electroreduction of flue gas CO_2 to formate using amine functionalized SnO_x nanoparticles (https://), ACS Energy Lett. 6 (2021) 3352–3358, https://doi.org/10.1021/acsenergylett.1c01553.